PUBLICATIONS OF THE ASTRONOMICAL SOCIETY OF THE PACIFIC, **120**:405–424, 2008 April

GROND—a 7-Channel Imager

J. GREINER, W. BORNEMANN, C. CLEMENS, M. DEUTER, G. HASINGER, M. HONSBERG, H. HUBER, S. HUBER, M. KRAUSS,[1] T. KRÜHLER, A. KÜPCÜ YOLDAŞ, H. MAYER-HASSELWANDER, B. MICAN, N. PRIMAK, F. SCHREY, I. STEINER,[2] G. SZOKOLY,[3] C. C. THÖNE,[4] AND A. YOLDAŞ

Max-Planck-Institut für extraterrestrische Physik, 85740 Garching, Germany; jcg@mpe.mpg.de, wab@mpe.mpg.de, cclemens@mpe.mpg.de, grh@mpe.mpg.de, hhuber@mpe.mpg.de, shuber@mpe.mpg.de, kruehler@mpe.mpg.de, ayoldas@mpe.mpg.de, H-M-H@mpe.mpg.de, b.mican@mpe.mpg.de, prima@mpe.mpg.de, fzs@mpe.mpg.de, yoldas@mpe.mpg.de

AND

S. KLOSE, U. LAUX, AND J. WINKLER

Thüringer Landessternwarte, Sternwarte 5, 07778 Tautenburg, Germany; laux@tls-tautenburg.de, klose@tls-tautenburg.de, john@tls-tautenburg.de

Received 2007 August 23; accepted 2008 February 01; published 2008 April 11

ABSTRACT. We describe the construction of GROND, a 7-channel imager, primarily designed for rapid observations of gamma-ray burst afterglows. It allows simultaneous imaging in the Sloan $g'r'i'z'$ and near-infrared JHK bands. GROND was commissioned at the MPI/ESO 2.2 m telescope at La Silla (Chile) in April 2007, and first results of its performance and calibration are presented.

1. INTRODUCTION

Simultaneous imaging in different filter bands is of interest in a variety of astrophysical areas. The primary aim is to measure the spectral energy distribution or its evolution in variable objects in order to uncover the underlying emission mechanism. Examples are, among others, (1) monitoring all kinds of variable stars (flare stars, cataclysmic variables, X-ray binaries) to determine the outburst mechanisms and differentiate between physical state changes and changes induced by geometrical variations, like eclipses; (2) monitoring AGN to understand the physical origin of the observed variability; (3) determining the inclination of X-ray heated binaries (Orosz & Bailyn 1997) (4) mapping of galaxies to study the stellar population; (5) studying multicolor light curves of supernovae (Taubenberger et al. 2006); (6) differentiating achromatic microlensing events (Paczynski 1986) from other variables with similar light curves; (7) identifying objects with peculiar spectral energy distributions, e.g., photometric redshift surveys for high-z active galactic nuclei, or identifying brown dwarfs; (8) follow-up observations of transiting extrasolar planets (Jha et al. 2000); or (9) mapping the reflectance of solar system bodies as a function of their rotation to map their surface chemical composition (Jewitt 2002).

A new need for multiband imaging arose with the observation of a large number of gamma-ray burst (GRB) afterglows with the *Swift* satellite (Gehrels et al. 2004). With its much more sensitive instruments, it detects GRBs over a very wide redshift range. Because intermediate to high-resolution spectroscopy to measure the physical conditions of the burst environment (e.g., Vreeswijk et al. 2007) is constrained to the first few hours after a GRB explosion, a rapid determination of the redshift became important. This is best done with multiband photometry (until integral field units have grown to several arcminute fields of view) and deriving a photometric redshift based on the Lyα break (Lamb & Reichart 2000).

Previous and current instruments with simultaneous imaging capability in different filter bands include A Novel Double-Imaging Camera (ANDICAM; two channels, one for visual, the other for near-infrared [Depoy 1998], presently operated at a 1.3 m telescope), Bonn University Simultaneous Camera (BUSCA; four visual channels [Reif et al. 1999], presently operated at the 2.2 m telescope at Calar Alto), High-speed Imaging optical Photometer for Occultations (HIPO; two visual channels [Dunham et al. 2004], to be operated on the Stratospheric Observatory For Infrared Astronomy [SOFIA]), Multicolor Imaging Telescopes for Survey and Monstrous Explosions (MITSuME; three channels with fixed bands g', R_C, and I_C [Kotani et al. 2005], operated at a 50 cm telescope), Triple Range Imager and Spectrograph (TRISPEC; three channels with one CCD and two near-IR detectors and wheels for filters, grisms and Wollaston prisms [Watanabe et al. 2005]), Simultaneous Quad Infrared Imaging Device (SQIID; JHK and

[1] Present address: ATV Technologie GmbH, D-85591 Vaterstetten, Johann-Sebastian-Bach-Str. 38; markus.krauss@atv-tech.de

[2] Present address: Ruhr-Universität Bochum, Astronomisches Institut, Universitätsstr. 150, 44780 Bochum; isteiner@astro.ruhr-uni-bochum.de

[3] Present address: Institute of Physics, Eötvös University, Pázmány P. s. 1/A, 1117 Budapest, Hungary; szgyula@elte.hu

[4] Present address: Dark Cosmology Center, Niels Bohr Institute, University of Copenhagen, Juliane Maries Vej 30, DK-2100 Kobenhavn; cthoene@dark-cosmology.dk

narrowband L filters in front of individual 512×512 quadrants of an ALADDIN InSb array, designed for the $f/15$ Cassegrain foci of the KPNO 2.1-m and 4-m telescopes [Ellis et al. 1992]), Ultrafast, triple-beam CCD Camera for high-speed astrophysics (ULTRACAM [Dhillon et al. 2007]; portable instrument that has been used at the Very Large Telescopes at ESO or the William Herschel Telescope, Canary Islands, as well as elsewhere).

Here we describe the design (§ 2) and performance (§ 6) of a 7-channel imager, called GROND (**G**amma-**R**ay Burst **O**ptical and **N**ear-Infrared **D**etector), which was specifically designed for GRB afterglow observations. We also mention some basics of the operation scheme (§ 3), related software (§ 4), and the changes to the telescope infrastructure which were implemented to use GROND for rapid follow-up observations (§ 5).

2. INSTRUMENT DESIGN

2.1. Scientific Requirements

The primary goal of identifying GRB afterglows and measuring their redshift led to the concept of a camera that allows observations in several filters throughout the optical and near-infrared regions at the same time. The simultaneity is dictated by the fact that a typical GRB afterglow fades by about 2–3 mag between 5–10 minutes after the GRB, and by another 4 mag in the following 50 minutes (e.g. Kann et al. 2008). Rapidly determining the photometric redshift of GRBs at $z > 5$ requires multiband photometry in at least 3–4 bands. In order to have a stable lever arm to determine (i) the intrinsic power-law slope of the continuum emission and (ii) the galactic foreground as well as GRB host intrinsic extinction, near-infrared bands up to K are essential. Extending the wavelength coverage beyond K by including, e.g., an L channel, was seriously considered during the design phase, but both the prospects of detecting a GRB in the L band as well as the substantial additional technical constraints due to the required lower temperatures led us to drop this possibility. Going as blue as possible is warranted by detecting the Ly-breakdown to redshifts of ≈ 3; however, also including a U or u' band turned out to be difficult due to space and logistics constraints. Leaving out one or two bands within our wavelength band would increase the error in the photo-z determination by a factor of 3 at least (for the redshift range covered by that band). Thus, we decided to use four bands in the visual, plus the standard JHK bands in the near-infrared (NIR).

The field of view (FOV) of the camera should be large enough to cover the typical error boxes of gamma-ray bursts, but on the other hand have a pixel scale less than the mean seeing to allow accurate photometry. Given the typical brightness of GRB afterglows, a reasonably large telescope with permanent access is another important requirement. Finally, as GROND would act as pathfinder to preselect "interesting" GRBs for more detailed follow-up observations, a nearby 8–10 m telescope was considered advantageous in the search for the final host telescope.

2.2. Optics

2.3. General Considerations

The final choice for the telescope was the MPI-owned 2.2 m telescope, operated by ESO on La Silla (Chile); see § 5. This telescope is a $f/8.005$ Ritchey-Chretien telescope (Ritchey 1928) with a focal length of 17,600 mm, on an equatorial fork mount; the intrinsic image quality is $0.4''$.

The prime goal for GROND is to investigate the high-redshift universe, thus emphasis was put on the NIR channels, and not on the visual ones. Consequently, it was decided to develop a focal reducer in the NIR with a $10' \times 10'$ field of view in order to cover GRB error boxes with a typical error radius of a few arcminutes (anticipated to occur about twice per week). In contrast, in the visual channels, no lens system was planned and the plate scale provided by the telescope optics was used.

The separation of the different photometric bands has been achieved using dichroics, whereby the short-wavelength part of the light is always reflected off the dichroic, while the long-wavelength part passes through. Thus, the first dichroics are used to split off the visual bands, which is done in the converging beam before the telescope focus. The relatively short back focal distance of 550 mm implied very tight constraints on separating the beams and still having enough space for the detectors. This, unfortunately, also prohibited using larger-format CCD detectors, because the consequently larger beams could not be separated further.

After passing a diaphragm at the nominal telescope focal plane, the beam is folded by 180° for space constraints, and fed into a collimator (Fig. 1, 2). The splitting of the three near-infrared channels occurs in the parallel beam between collimator and camera objective of the NIR focal reducer.

One might expect different ghosting effects in the visual arm (dichroics in converging beam) and the near-IR arm (parallel beam). While it is true that reflections from the back surface of the dichroic in the parallel beam produce ghosts that are not offset relative to the main image, the effect of these ghosts is negligible. Both the dichroic as well as the antireflection coatings have efficiencies of about 99.5% in their transmitting regions. Since back surface ghosts involve two coating passages, they arrive with $< 0.0025\%$ (corresponding to 11 mag fainter) of the original intensity, undiscernable in data analysis.

Another typical concern of dichroics is their polarization-dependent location of the cut wavelengths, in particular since gamma-ray burst afterglow emission shows variable optical and NIR polarization. We have therefore embarked on a dedicated study of this effect prior to the coating of the optics. While standard cut wavelengths differ by 7% (3–4%) for dichroic cubes (plan-parallel plates) between the perpendicular polarization directions, the final GROND coatings only have a difference of 1% (e.g., 15 nm for the JH dichroic coating). For a 100% polarized white light beam this leads to a $\lesssim 0.1\%$ change

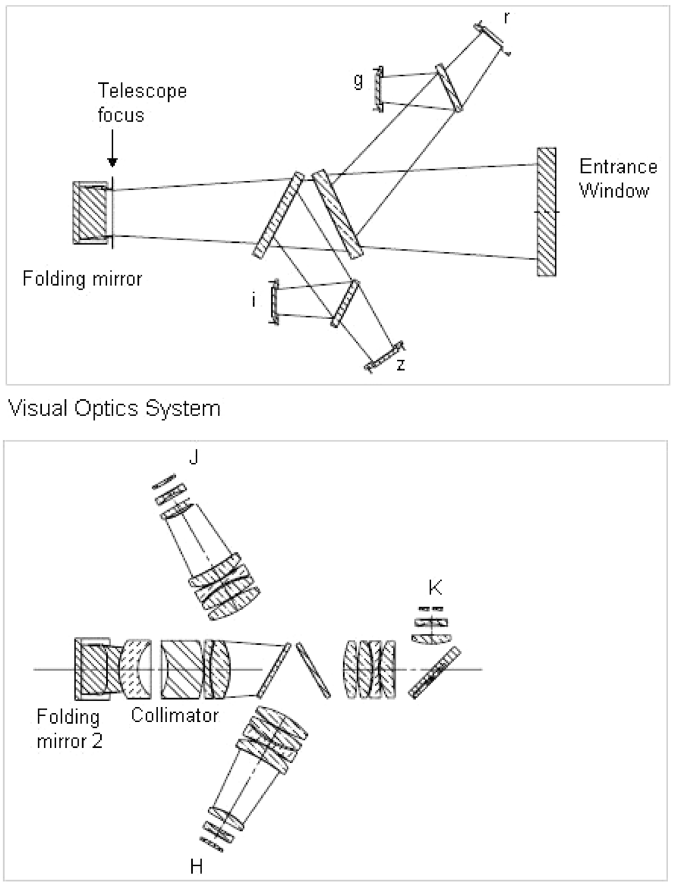

FIG. 1.—Layout of the of GROND optics with the top panel showing a cut through the visual arm and the bottom panel a cut through the NIR arm.

in the transmitted flux, which in turn implies a $\lesssim 10^{-3}\%$ change in the color terms (see § 6.2), and thus is tolerable.

The entire system has been designed for a working temperature of 80 K in vacuum, because deviations from the nominal temperature by more than 20° would lead to refractive index changes large enough to cause noticeable image quality degradation, and we considered it too risky to predict an equilibrium temperature gradient between the visual and NIR parts. Since the mechanical assembly was done at room temperature, all optics (and mechanical) system parameters had to be calculated for a temperature of 80 K. For example, the focal length of the focal reducer differs by 3 mm between 293 K and 80 K, compared to a depth of focus of 25 μm. We imposed a high accuracy requirement on the mechanical support structure, so that an alignment of the optics system is only required along the optical axis.

2.3.1. The Four Visual Channels

For the visual channels the incoming 1:8 telescope beam is split using 4 dichroics (top panel of Fig. 1). The field of view is determined by the telescope focal length (17.6 m) and the size of the CCDs ($2048^2 \times 13.5$ μm). For each CCD the field of view is 5.4×5.4 arcmin^2, and the plate scale is $0.158''$ pixel^{-1}.

All four CCDs are backside illuminated E2V devices without antiblooming structures and are operated in inverted (AIMO) mode. The chips come on nickel-plated ceramic base plates. Since each of the detectors serves in one and only one filter band, different sensitizations of the detectors have been applied: g': astro-broadband on normal silicon, r': midband on normal silicon, i' and z': basic-NIR on deep-depletion silicon.

The use of dichroics implies that adjacent bands have identical 50% transmission wavelengths, making the Sloan filter system (Fukugita et al. 1996) the obvious choice. Thus, the dichroics were designed such that the combination of their cutoff wavelengths define bands identical to the Sloan system, with the exception of the i' band. Since in the Sloan system $r'i'z'$ overlap at their ~70% transmission values, we decided to compromise the i' band in favor of standard-width r' and z' bands.

The telescope beam is first split by reflecting off the g' and r' bands, then the i' and z' bands. The long-wavelength part of the beam (the NIR part) is then passed through the primary cold stop in the focal plane. Two further dichroics are placed into each of the two visual beams to separate g' and r', and i' and z', respectively. The dichroic plates are wedge shaped by ~13–19 arcmin so that they compensate for the astigmatism of a plane-parallel plate in the converging 1:8 beam of the telescope (Woche et al. 2000). The curvature of the focal plane of the telescope has a radius of 2205 mm, which corresponds to a focus difference of 43 μm between the center and edge of the CCD. This is smaller than the depth of focus of ~60 μm at the shortest wavelength used, but of course causes astigmatism (see Fig. 3).

Originally, no other optics were planned except for the dichroics. After first light it became apparent that the g' and i' bands suffered from single reflections of r' and z' light, respectively, off the backside of the dichroics, at a strength of about 0.5% of the incident intensity. Thus, each of the CCD channels has been equipped with a short-pass filter to block these single reflections. The backsides of those 3 mm glass filters have antireflection coatings at $>99.5\%$ efficiency, except for the g' band (see below).

Another post-commissioning change has been implemented for the g' band: originally, no short-wavelength cutoff was foreseen, since we expected the transmission of the telescope mirrors and the entrance window as well as the efficiency of the CCD detector to fall off rapidly enough below ~400 nm. In fact, the ill-defined cutoff led to a photometric uncertainty of about 5% which was deemed unacceptable (see § 6.1). We therefore implemented a short-wavelength edge filter with a cutoff wavelength of 380 nm.

2.3.2. The Near-Infrared Channels

The NIR part is designed as a focal reducer system allowing for an optimized adjustment of the focal length, or equivalently

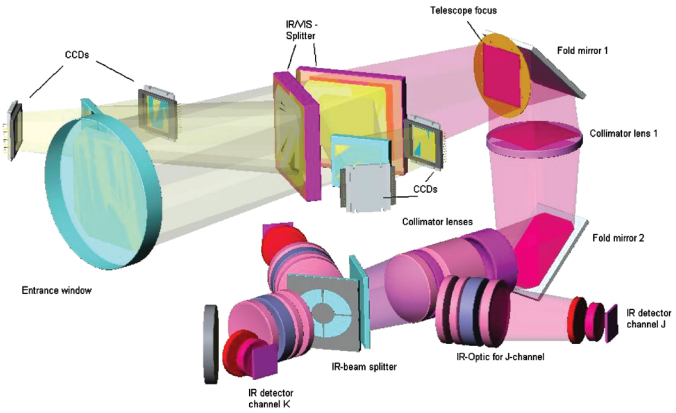

FIG. 2.—Visual and NIR beams' 3D structure with most of the components labeled.

the field of view. In this way the required 10′ FOV is imaged onto a 1024×1024 Rockwell HAWAII-1 array (pixel size 18.5 μm, plate scale of $0.60''$ pixel^{-1}). The focal reducer system (5 collimator lenses with a resulting $F_{coll} = 360$ mm and 6 camera lenses with $F_{cam} = 129.6$ mm for each NIR channel) has a pupil reduction factor of 48.89 and a pupil diameter of 45 mm. For the $f/8$ telescope the resulting effective focal length is 6336 mm.

A diaphragm is placed in the telescope and collimator focus, including blocking of the M2 mirror and M2 spider structure. The two beam splitters for reflecting off the J and H bands are located in the parallel beam of the focal reducer, between collimator and the camera objectives (Fig. 1, 2). In addition, each channel has a cold pupil stop near the dichroic, as well as a filter in front of the first camera lens defining the standard JHK bands (which also prohibit long wavelengths' single reflections to reach the detector). The JHK filters differ from canonical NIR filters in their much reduced blocking range, which is sufficient for GROND because of the action of the dichroics. Thus, the mean transmission in the JHK bands (including dichroics) is $\gtrsim 98\%$.

Because of the parallel beam, the dichroics could be manufactured as true plane-parallel plates and mounted in a compact 60° box that allows for a space-saving splitting of the beam into the J, H, and K channels. The K channel includes an additional flip mirror for dithering purposes.

The focal reducer system designed for GROND differs substantially from that of other optical focal reducer systems (e.g., the Calar Alto Faint Object Spectrograph CAFOS,[5] the Multi Object Spectrogragh for Calar Alto MOSCA[6], or the Potsdam Multi-Aperture Spectrophotometer PMAS Roth et al. 2006

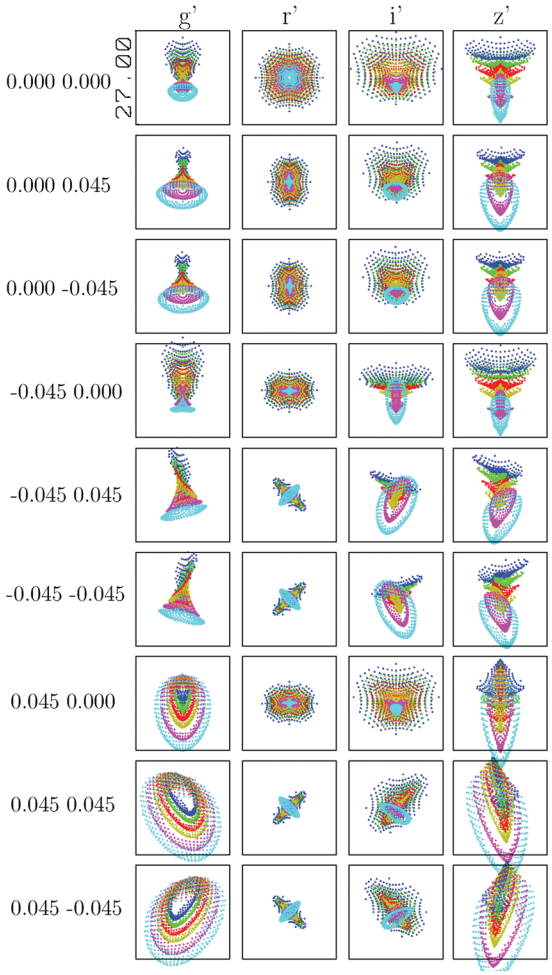

FIG. 3.—Spot diagram of the four visual channels at different off-axis angles (*rows*): the numbers on the left give x and y coordinates in degrees within the field of view, the top row corresponding to the optical axis. It shows the geometrical aberrations (without diffraction) in the focal plane. The wavelength range of each band is simulated with three individual wavelengths. The nonsymmetrical images are due to the wedge shape of the dichroics. Note that the r' channel only involves reflections from the dichroics, and therefore is symmetric (and, thus, shows the image quality provided by the three mirrors of the telescope). Each panel is 27 μm × 27 μm, corresponding to 2 × 2 pixels of the detector.

at Calar Alto), because no optical glasses could be used. Basically, only four media are available for transmission in the 900–2400 nm range: CaF_2, BaF_2, OH-free Silica, and undoped YAG. Because of its transmission characteristics, YAG is particularly suited for NIR optics (but also difficult to grow in large dimensions). Using these four optical media, and after measuring their refractive indices at the foreseen operational temperature of 80 K, the focal reducer system could be designed with a high performance (Fig. 4) using software developed by us (Laux et al. 1999). The 3D visible and NIR

[5] For more information on CAFOS, see http://www.caha.es/CAHA/Instruments/CAFOS.

[6] For more information on MOSCA, see http://w3.caha.es/CAHA/Instruments/MOSCA.

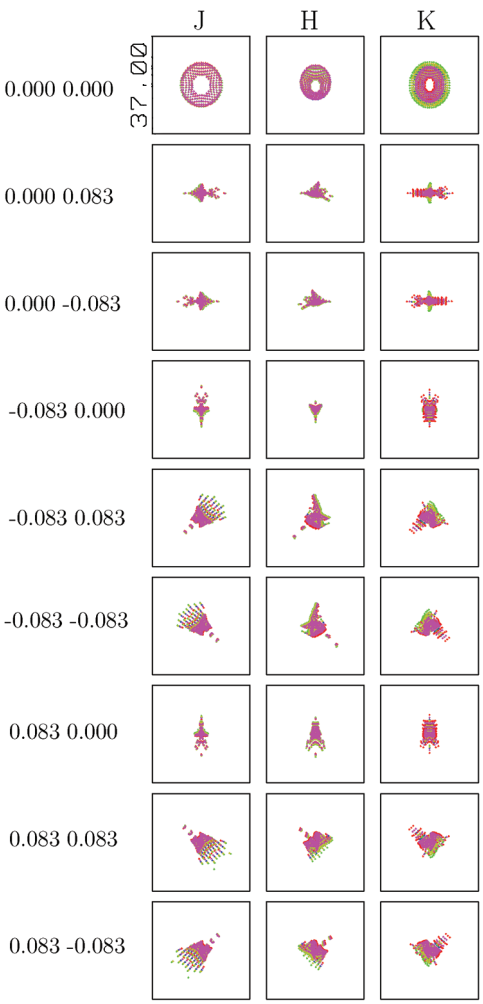

FIG. 4.—Same spot diagram as Fig. 3 but for the three infrared channels. The focal reducer was designed to optimize the image quality (point source shape), but still contains image distortions, i.e., plate scale changes depending on the position in the focal plane. These geometrical distortions are corrected during the data reduction process (see § 4.3). Each panel is 37 μm × 37 μm, corresponding to 2 × 2 pixels of the detector.

model as well as the optics components CAD files were created using the ZEMAX software package[7].

2.4. Cryo-Mechanics

2.4.1. Cryostat

The GROND cryostat (Fig. 5) consists of the following components: (a) GROND-cylinder, made of titanium, and electron beam welded; (b) the front and back plates made of aluminum; (c) 4 spacer rods; (d) 8 Belleville-spring systems; and (e) O-ring seals (Viton).

[7] See the ZEMAX Development Corporation's Web site at http://www.zemax.com.

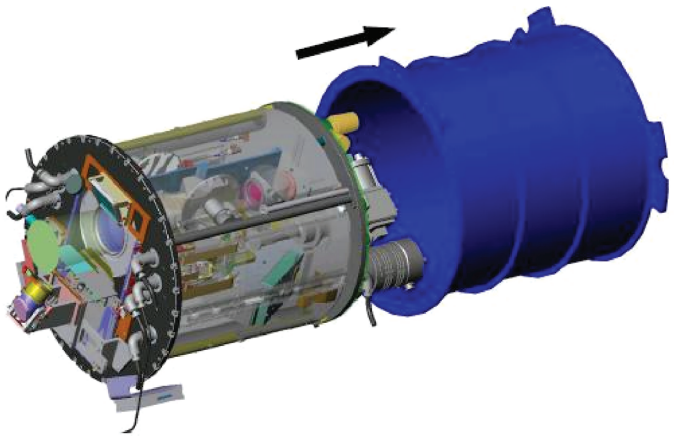

FIG. 5.—Removing the cylindrical shell of the cryostat allows easy access to all internal components.

The components inside the GROND cryostat have different thermal requirements. In addition, in the case of single component failures, no sensitive components should be exposed to dangerous thermal conditions. The complete internal structure is mounted on a titanium alloy (TiAlV) plate that provides thermal insulation. This plate is mounted on the front plate of the cryostat, which accordingly becomes the nominal reference point of the system. As the different components (front plate, titanium plate, optical bench) have different temperatures, the mounting must allow for thermal contractions. This is achieved by using long holes and centering pins to mount the titanium plate. The internal components (optical benches) are connected to the back plate of the cryostat using a metallic membrane that allows contractions only along the optical axis of the instrument.

The cooling system is based on a two-stage Sumitomo Closed-Cycle Cooler (CCC) with a SRDK-408-S cold head which provides a cooling power of $\gtrsim$35 W down to 45 K at the warm stage, and $\gtrsim$6.3 W down to 10 K at the cold stage. The cold head is mounted using a bellow (to reduce vibrations) on the back plate of the vessel.

The first stage of the CCC (higher temperature and higher cooling power) is used to cool the optical benches (visual and near-IR) and all optics components to 80 K (temperature-controlled). The second stage (lower temperature and lower cooling power) is used to cool the near-IR detectors to 65 K (optimum temperature to maximize the signal-to-noise ratio). The CCD detectors have an intentionally bad thermal connection to the visual optical bench (80 K). They are stabilized at 165 K using resistor heaters. Thermal connections between the two baseplates and the components are realized using copper flanges, copper ledges, and flexible copper lines. Galvanic isolation of the cooling system is achieved by isolation foils being mounted between the thermal copper flanges and the CCC stages.

To reduce the thermal input, the optical benches are thermally insulated from the cryostat. In addition, thermal shields are installed to reduce the radiative heat transfer. The main

radiation shield is between the optical benches and the vessel. It is thermally insulated from both. The radiation shield is constructed of three round plates (two at the front plate, one at the back plate of the vessel), four half cylinders around the spacing bars, and six dismountable cylinder segments—all made of 1.5 mm thick highly reflective aluminum plates. The cylinder segments are additionally covered with multilayer insulation foil.

2.4.2. Structural Chassis

The implementation of the optical requirements with the geometrical and mechanical constraints such as tight space, minimum weight, and different temperature regions within the main housing resulted in substantial complexity, which in turn required most subunits and their interrelations to be treated simultaneously. The development of the optical-mechanical configuration included considerations such as: (i) space requirements for the 4 CCD cameras and 3 NIR-detector units, (ii) use of structural components, such as optical benches, mounting interfaces/connections, and cold connections, (iii) assembly and handling procedures, (iv) cabling, and (v) low-temperature–induced contractions interacting in 3 dimensions.

The final structural chassis (Fig. 6) consists mainly of two separate optical benches. The top bench (Fig. 7) contains the optical and mechanical groups for the visual light detection, in particular: (1) the entrance light baffle (not shown in Fig. 7); (2) principal light splitter unit with two dichroics; (3) small dichroics splitting the g', r' and i', z' channels; (4) two VIS-shutter units for CCD channels $g'r'$ and $i'z'$; (5) all four CCD boxes for $g'r'i'z'$; (6) NIR channel shutter to close the NIR sector completely; and (7) mirror carrier unit for folding mirror 1 (also not shown in Fig. 7). The lower bench (NIR area; Fig. 8) contains the following components: (1) second folding mirror (adjustable in 3 degrees of freedom); (2) collimator lens unit; (3) two NIR

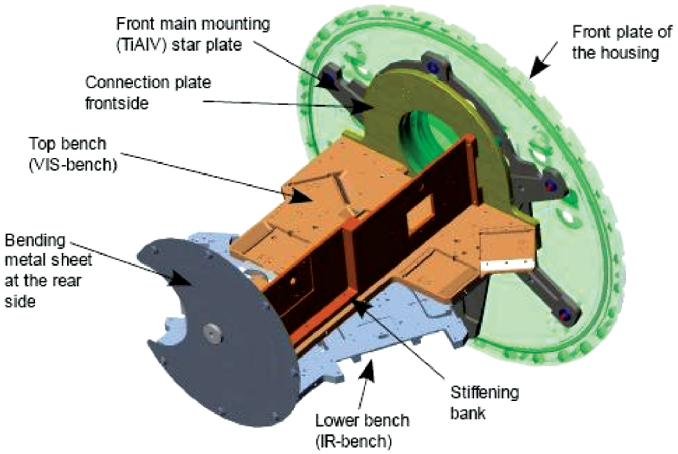

FIG. 6.—GROND structural chassis with the two separate optical benches (visual in orange, NIR in blue) and the main aluminum alloy front plate (gray spider plate).

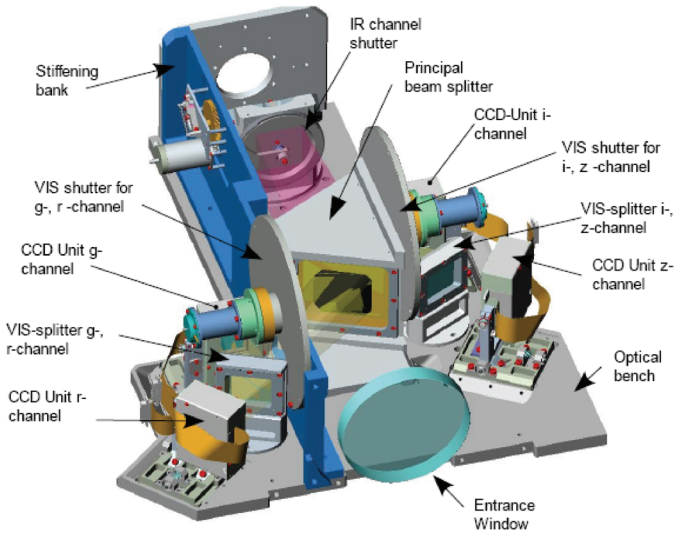

FIG. 7.—Visual base plate with nearly all optical and mechanical components marked.

beam splitters to separate J, H, and K; (4) one camera lens system (split into two mechanical lens holders; Fig. 1); for each of the 3 NIR channels; (5) dithering mirror unit for the K-channel; (6) NIR-detector units (motorized for focusing); (7) Zeolith boxes near the CCC cold stage as water (humidity) sinks (not shown in Fig. 8). The NIR light path is only open at the focal plane, but otherwise completely closed by a dedicated light-tight housing cooled to 80 K. Cabling is done through light traps.

2.4.3. Lens Mounting

Within the focal reducer, 23 lenses are maintained at precise position during the cooling to 80 K. A special spring-based

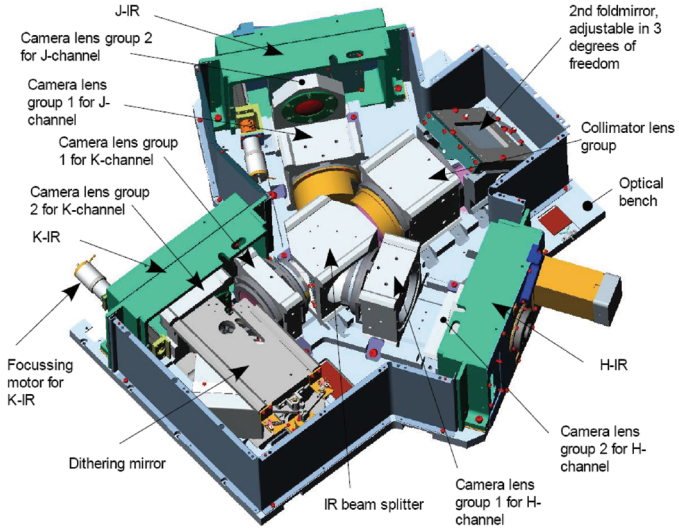

FIG. 8.—Infrared base plate with all optical and mechanical components.

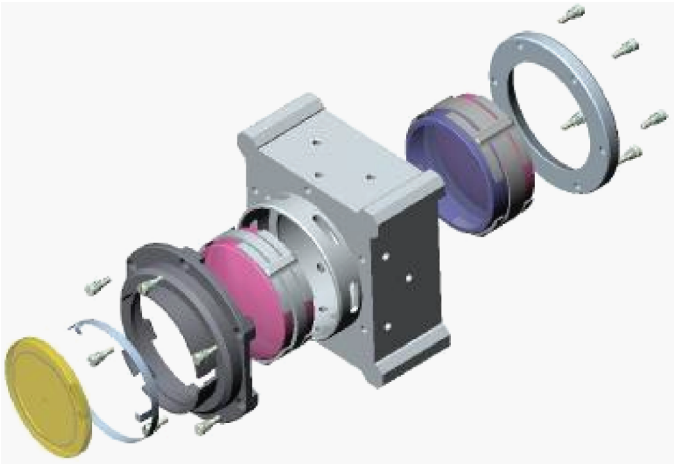

FIG. 9.—Exploded view of the lens mounting block for the four collimator lenses in each of the three NIR channels.

lens-mounting design was developed (Fig. 9) that keeps the lenses centered and in the correct axial position. During the cooling, the radial flexibility of the lenses is kept small enough to ensure the required centricity.

2.4.4. IR Unit

The tight space constraints also made it necessary to develop a new, much smaller detector board (shrinking from 220 mm diameter originally to a square of 50×70 mm). Consequently, the mechanics also had to be redesigned from scratch, and the opportunity was taken to implement two new features: (i) motorized positioning of the detector along the optical axis, and (ii) a gimbal mounting to allow manual alignment of the detector plane perpendicular to the optical axis in both degrees of freedom (Fig. 10).

A cold finger on the backside of each NIR detector is directly connected with the second stage of the CCC, thus allowing the NIR detectors to cool below the temperature of the baseplate and optics. Since the CCC temperature is load dependent, a heater is installed on the cold finger to control the temperature and keep variations below ± 0.1 K.

2.4.5. CCD Detector Unit

The CCD detector units have no motorized focusing stages, because the depth of focus is larger. Still, they can be aligned in 4 degrees of freedom (Fig. 11). Because the minimum allowed operational temperature of the CCDs ($\sim$155 K) is much higher than the inner cryostat temperature, the CCDs are equipped with a heat finger and thermally controlled via the PULPO electronics (see § 2.6.2) to 165 K within ± 1 K.

2.5. Cryo-Motors

There are several motorized mechanisms in the instrument that operate at 80 K. All motors are from Phytron, but use different gears.

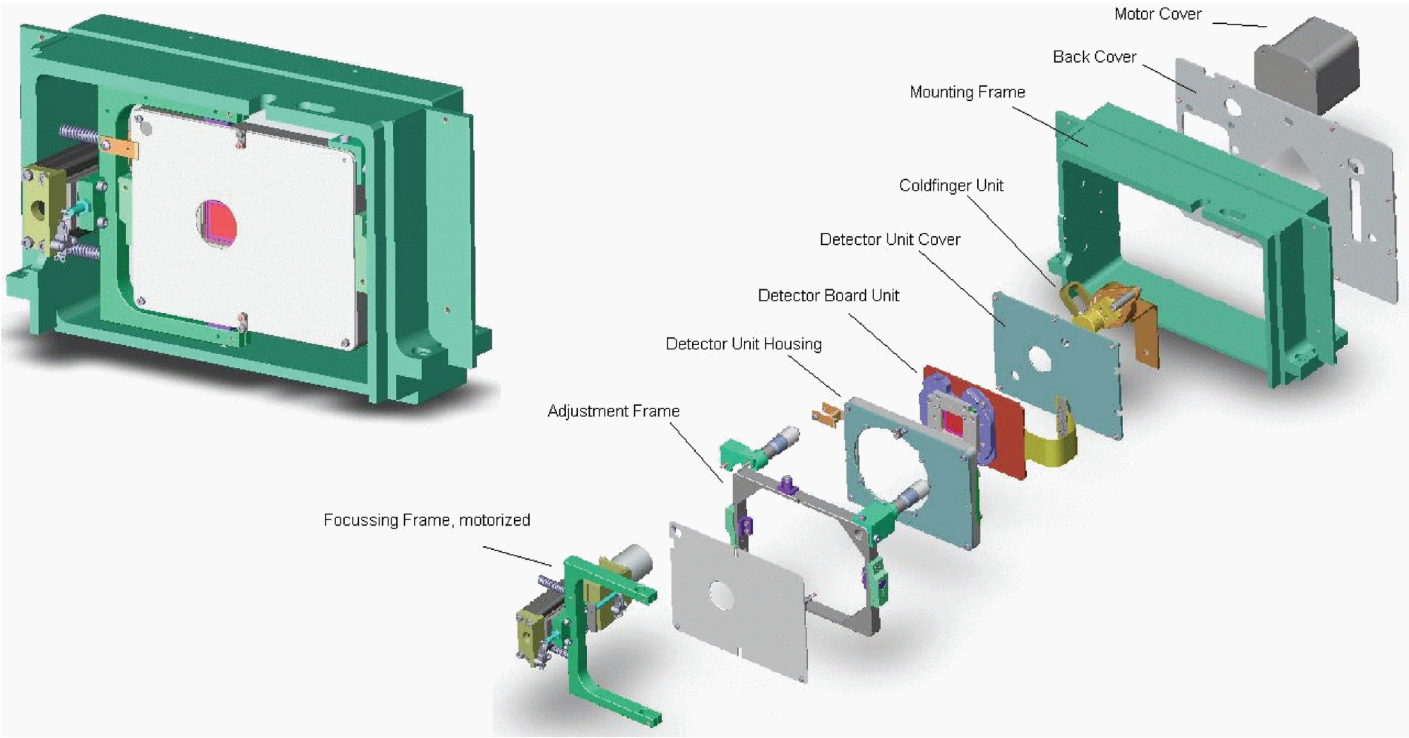

FIG. 10.—Schematics of the NIR-detector unit.

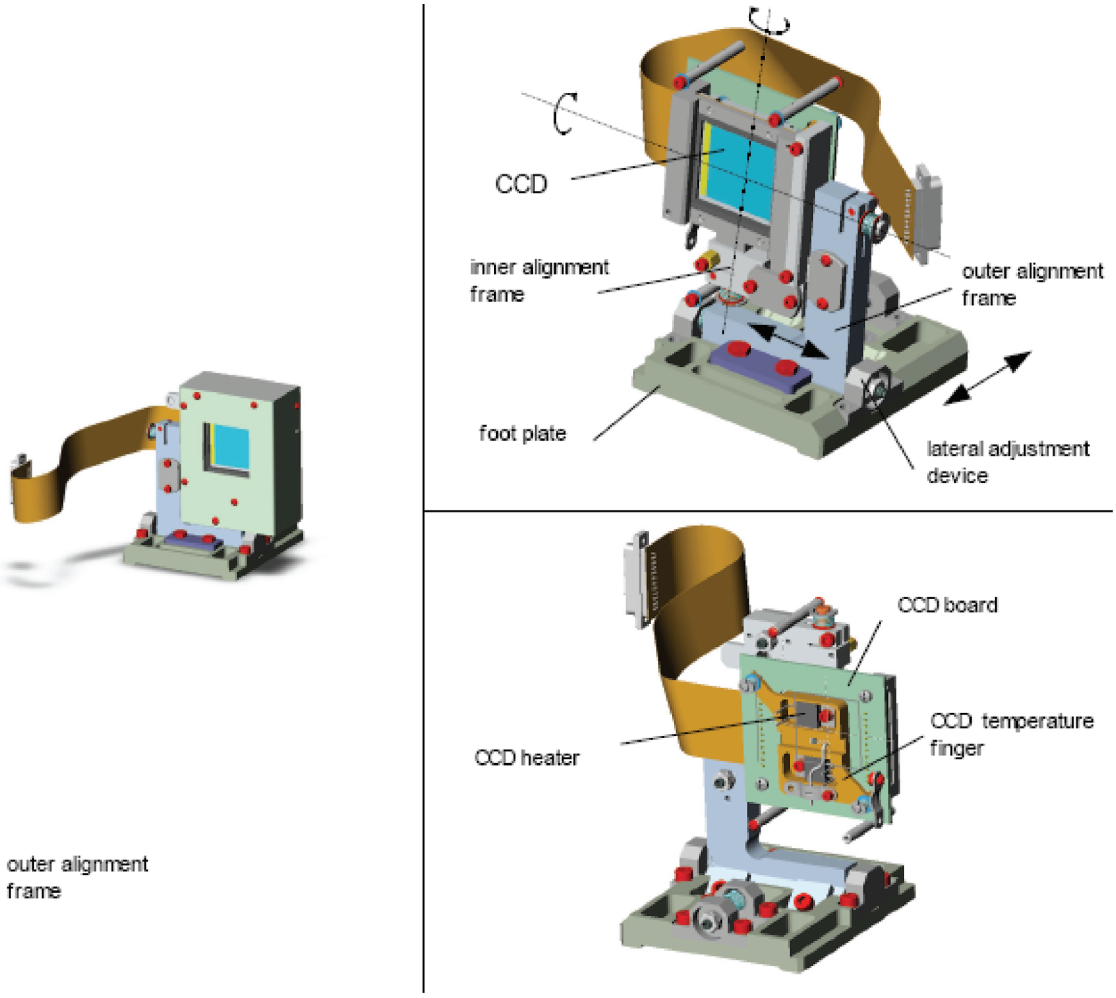

FIG. 11.—Schematics of the CCD-detector unit. The arrows denote the alignment possibilities.

1. *NIR channel Shutter*: This door closes the NIR arm of the instrument, so one can take darks in J, H, and K. It is implemented using a stepper motor.

2. *Visual Shutters*: Due to the constraints of the optical design of the instrument, the CCD shutters must be cryogenic (as the shutter must not block the infrared channels). Due to the tight space constraints, one shutter per CCD was mechanically impossible; thus two shutters have been implemented, one for the $g'r'$ and one for the $i'z'$ channels, respectively. Each shutter is a thin metal disk with two quadrant shaped openings at opposite sides that are slightly larger than the beam at this position. Thus, each disk has two "shutter closed" and two "shutter open" positions, i.e., 4 possible positions in total that are 90° apart. Each shutter is equipped with a stepper motor and a position encoder that provides the (absolute) position of the disk. The combination of stepper motors and encoders ensures that movements are fast (with stepper motors one can 'blindly' move the shutter by 90°) and that the shutter does not drift over time, resulting in vignetting (i.e., the 4 nominal positions are tied to encoder positions). This design is still slightly slower than typical, noncryogenic shutters, but it is fast enough (below 1 s) for typical exposure times of 1 minute or more. The two shutters can be operated independently; thus, different integration times in the two optical arms are possible. Shutter movement is triggered by the PULPO shutter control port (see § 2.6.2).

3. *Flip mirror zero position*: The flip mirror (K-band channel dithering) can be either in the calibration/alignment position (i.e., no dithering) or in the normal position (where dithering is possible by rotating the flip mirror). This function is implemented using a stepper motor that moves the mirror into either position.

4. *Flip mirror dithering*: This motor is responsible for the internal dithering in the K band. Dithering in K as opposed to the other channels is required due to the high sky brightness. In order to allow staring at the same sky position in the optical bands (because of the long CCD readout times), this internal dither mirror has been implemented. The dither function is

implemented using a CLD stepper motor linear drive from Phytron and an encoder. Two fundamental operational modes are implemented. Either the motor is moved to an absolute position, or the motor moves in either direction 45, 60, or 90° (i.e. 8, 6, or 4 dither positions).

5. *IR focus*: Each of the three NIR detectors can be focused independently using 3 stepper motors with gears. Each motor allows relative movements to the required accuracy of ± 25 μm), over a range of ± 2 mm. The gear is strong enough to prevent any shift of the NIR detector with positioner in the best-focus position during telescope movements.

2.6. Electronics

The electronics are divided into several parts: (i) the main rack which contains the GROND-specific control, (ii) the readout electronics for the CCD and NIR detectors as provided by ESO.

2.6.1. Main Electronic Rack

2.6.1.1. Interface unit and main control

This unit forms the control interface between the GROND instrument workstation and the motor control electronics. The main part of this unit is a XILINX FPGA, which makes the electronics more flexible. Each IO of this XILINX FPGA is driven by a bidirectional bus driver and additionally ESD protected by a low capacitance diode array. The current design uses 98 pins for input and 66 pins for output purposes, with 32 spare pins.

Communication interface: The communication interface is realized by an onboard RS232 interface with two jumpers for speed selection. The nominal operation speed is 115,200 baud. A RS232 server converts this signal to 100baseT for the instrument workstation. To maximize reliability, a special command structure is used. After the detection of the sync byte, the interface unit starts a time-out counter. If a command is not completed within 8 ms, this command will be rejected and the whole communication unit reset, so that this unit can receive new commands immediately. This protects the system from hanging due to incomplete commands.

Motor Control: The main control contains all electronics necessary for the digital control of the motor driver boards and position readout. All signals that are important for operation of the motor driver electronics (clock, boost, direction, reset), are delivered by the main control. For all position-switch controlled stepper motors (IR calibration, cold shutter, zero position), the digital circuit prevents a motor overrun (i.e., an end switch). This means that as long as the stepper motor is between the two end switches the direction will be determined by the user. If one of the end switches is reached, the motor stops immediately and the direction is automatically reversed. Likewise, these electronics are responsible for the readout of the resolver values and synchronization with the stepper motors. Three resolvers are controlled by the GROND electronics; one for the flip mirror and two for the CCD shutters.

An additional offset register can be used to calibrate the start position of the flip mirror. The movement is bidirectional and commandable. The accuracy of the flip mirror position is about 5.4 $'$ (4000 steps per full rotation). Contrary to the flip mirror, the CCD shutter electronics have only one mode ($4° \times 90°$). The shutter is commandable over the PULPO (see § 2.6.2) interface, which gives a single bit state to the shutter electronics that determines whether it is open or closed. A commandable offset register for each CCD shutter helps the user to adjust the initial open/close position. The accuracy of the shutter is also 5.4 $'$, corresponding to 80 μm in the center of the opening.

2.6.1.2. Motor driver boards for stepper motors

The motor driver board has two independent driver units. These boards are used for driving the NIR focusing stage, the cold shutter, and the zero-position motors. Each driver unit has four current modes (boost, run, standby, off), which are selected via two status bits. The current levels for the modes can be set using variable onboard resistors. Additionally, each driver unit has its own temperature sensor, which prevents overheating.

2.6.1.3. Motor driver boards for linear motors

This board was specially developed for high current with linear motors. Linear motors are used for moving the M3 mirror and the main shutter door in front of the entrance window. The board works with two limit switches, between which the motor can move. The forward–backward movement of the mirror is possible by software-controlled command (from the GROND instrument workstation) or manually over a special control box at the telescope's M1 mirror cell.

2.6.1.4. Resolver boards

An AD2S82A represents the main part of the resolver board, which is a variable resolver-to-digital converter. The resolution of this converter is variable and can be set up to 16 bit, which means that a maximum resolution of approximately 20″ is possible. The sine-wave for the LTN resolver is produced by the maximum high frequency waveform generator Max038. This produces an optimal signal for the resolver. A high-speed voltage follower is connected at the outlet side to provide a high current driver for long cables. Likewise the offset of the sine-wave can be adjusted with a voltage buffer. All resolver boards used in the GROND electronic rack have the following configuration: resolution: 16 Bit; peak-to-peak sine wave amplitude: 2 V; frequency: 10 kHz; offset: 0 V.

Finally, the primary power of all motor power supplies is switched on by a zero-crossing switch. This prevents a high inrush current on the main power line during switch on.

2.6.1.5. Temperature control

The electronic rack has two temperature control systems. The temperatures of the NIR-detector system is monitored by Lakeshore temperature controllers. Each of the three NIR detectors has its own Lakeshore controller LS331,[8] which in turn has two control loops: Loop1 with 50 W maximum heating power is used to warm up and regulate parts of the baseplate. Loop2 with 1 W maximum heating power controls the detector temperature with an accuracy of $\pm 0.1°$. The nominal operating temperature of the GROND NIR detectors is 65 K.

For the optical CCDs, temperature sensors and controlled heaters are directly mounted to the CCD detector backside and controlled via PULPO (see § 2.6.2). Because each PULPO can control only one shutter, two PULPOs are incorporated in the electronic rack. The nominal heating power of the PULPO is 7 W in each circuit. For safety reasons, the power at the CCDs was reduced to 1 W. A third heater, also controlled by each PULPO, is mounted on each of the two clock-bias board thermal shields, with 7 W heating power.

2.6.2. Detector Readout Electronics

IRACE: The readout system for the infrared detectors, the Infrared Detector High Speed Array Control and Processing Electronics (IRACE; Meyer et al. 1998) system, was supplied by ESO. As readout mode (IMODE), the double-correlated mode is used, as it is the only valid mode for science observations. One change was made to the basic IRACE system, namely to read out all three detectors simultaneously and store the data into one FITS file.

FIERA: The Fast Imager Electronic Readout Assembly (FIERA; Beletic et al. 1998) system was also provided by ESO. Implemented changes include (i) independent readout for two pairs of CCDs and (ii) a 3.8 m instead of the nominal 1.8 m cable to the front-end electronics (which does not increase readout noise). For GROND, the two-port readout of each detector is used, and one FITS file with four separate extensions is written after each exposure (the two readout ports are combined into one image before writing to file). Furthermore, two readout speeds are typically used: the fast mode (625 k pixel s^{-1}; readout noise of ≈ 23 e^-) in the 4 minute and 6 minute observation blocks (see below), and the slow mode (50 k pixel s^{-1}, ≈ 5 e^-) in all longer observation blocks. The FIERA system includes PULPO (Hadad & Sinclair 1998), a separate electronics box used to measure and control temperatures (via three heaters), measure the vacuum in the cryostat (two inputs), and to operate one shutter.

3. GROND OPERATION SCHEME

The GROND operation scheme is designed to be as generic as feasible, but primarily suitable for prompt, automatic GRB follow-up observations. Additionally, it should provide the basic functionality to perform observations of any other nontransient object. However, operating a 7-channel imager in a single cryostat implies various observational constraints that should be considered in the creation of the observation blocks (OBs; Chavan et al. 2000). Each observation is built by combining exposures (differing in number and length) of the seven detectors based on an appropriate set of parameters. This approach provides the most generic background for science observations with the current instrument design. The most important parameters are the number of telescope dither positions NTD, the number of telescope pointings NTP, the number of exposures in the g' and r' band NGR, the number of exposures in the i' and z' band NIZ, the corresponding integration times UITGR and UITIZ, the number of K mirror dither positions NMD, the number of K mirror pointings NMP, the number of JHK exposures in a single K mirror position NINT, the number of stacked JHK exposures NDIT, and the JHK integration time DIT.

In order to comply with the GROND science objectives, different default OB types are defined for autonomous observations of GRB afterglows. The OBs are named after the total integration time in the K band, namely 4-, 8-, 20-, and 40-minute OBs, all with four different telescope dither positions, as well as 6-, 12-, 30-, and 60-minute OBs with six telescope dither positions.

All parameters for GROND observations can be adapted for use in nonstandard OBs, within their constraints as described above. However, all bands and their readout have to be synchronized for telescope dithering, which means that the integration time of the optical bands must be adapted to the parameters of the infrared observations (and/or vice versa). For nonstandard OBs, this remains the responsibility of the user.

By default, one standard OB consists of four or six telescope dither positions: NTD = NTP = 4 or 6, each with six K band mirror dither positions (NMD = NMP = 6). A total of NINT = 1 , 2, 5, and 10 single J, H, and K integrations are possible at each K mirror dither position.

A generic breakdown of the shortest 4-minute OB and the underlying structure in a single telecope dither position can be seen in Figure 12. Schemes for the other default OBs differ in the number of J, H, and K integrations (NINT) and telescope ditherings (NTD), and the CCD detector readout mode (OMODE).

4. SOFTWARE

4.1. Instrument Software

The GROND instrument software is based on the standard ESO/VLT software environment.[9] The CCD detectors are handled as a normal array of four chips, each with 2-port readout. The single FIERA controller drives all four chips. The two shutters are operated in parallel. In order to integrate longer in the bluer ($g'r'$) channels, two special readout modes were intro-

[8] Lakeshore's Web site is http://www.lakeshore.com/temp/cn/331dn.html.

[9] More information on the VLT Sofware can be found at http://www.eso.org/projects/vlt/sw-dev.

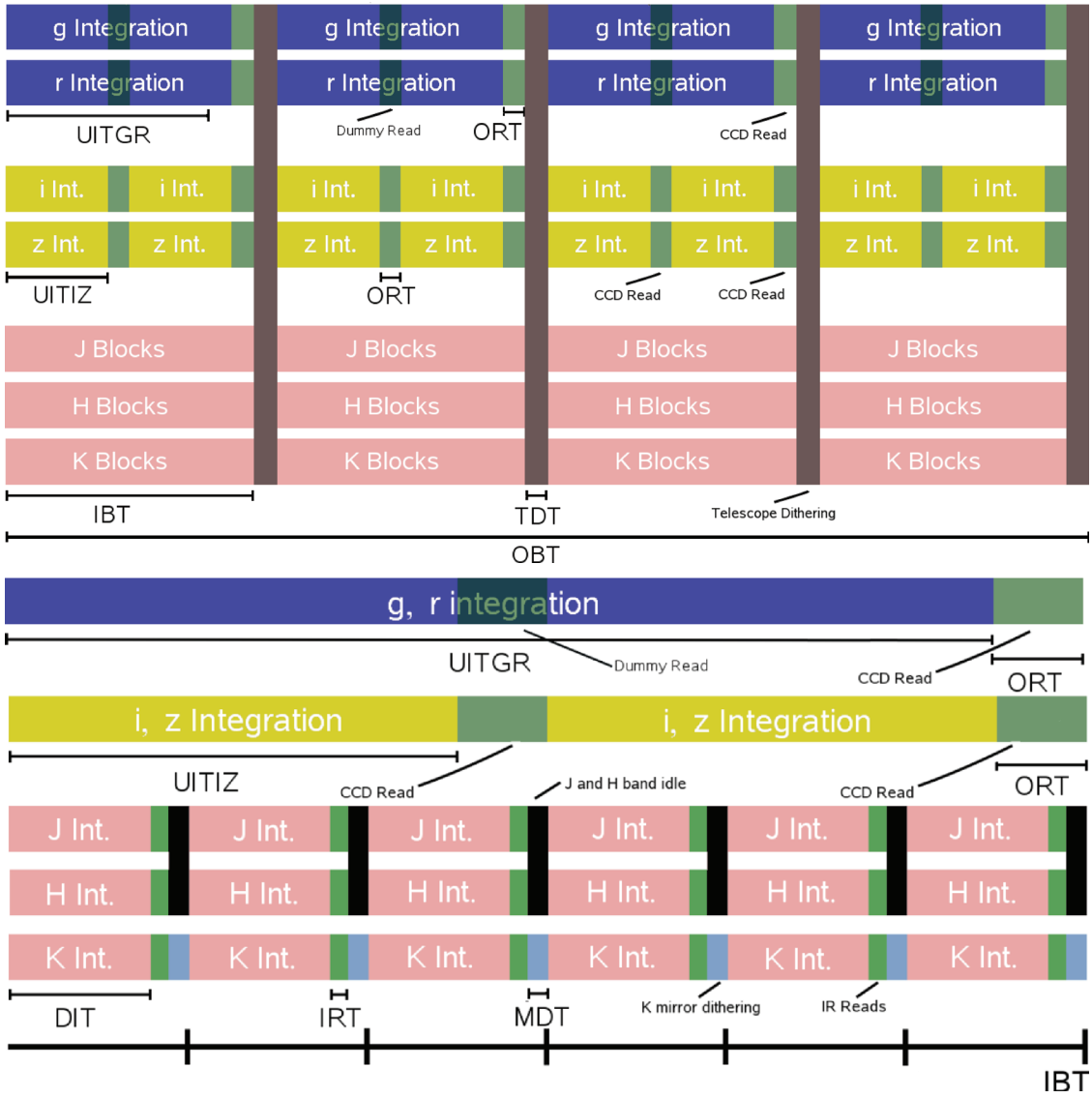

FIG. 12.—*Top:* Overview of the shortest generic 4-minute observation block for the FIERA configuration, i.e., the CCD exposures. The readout (r.o.) of the detectors should not overlap with telescope dithering, as it adds substantial noise to the data. The parameters of the shown 4-minute OB are: NTD = 4, NGR = 1, NIZ = 2, and OMODE = 0 (625 k pixel s^{-1}). With two exposures in the $i'z'$ channels during one exposure in the $g'r'$ channels, the data in $g'r'$ are not readout, but an (empty) FITS file is created (so-called dummy readout). Descriptions in the image apply to all equally colored regions (ORT ≡ CCD readout time, TDT ≡ telescope dithering time, IBT ≡ duration of a single infrared block, and OBT ≡ duration of the whole observation block). *Bottom:* Substructure of the observation blocks for the infrared exposures. The readout of infrared detectors has to be separated from the K_S mirror dithering. The parameters underlying the shown substructure of infrared blocks are NMD = 6, NINT = 1, and IMODE = 0 (double-correlated readout). (IRT ≡ infrared detectors read out time, MDT ≡ K mirror dither time.)

duced: one that drives only the $i'z'$ CCDs (i.e., one can read out only these two chips while leaving the image in the other two intact) and a second readout where the $g'r'$ chips are not wiped or reset at the start of the exposure. When combined, these two readout modes allow a special operation mode where one takes one $g'r'$ image for every two $i'z'$ frames. Thus, in the bluer channels the efficiency is significantly improved due to the additional exposure time. There is a resulting trade-off between the dark time (between reset/wipe and readout) and the exposure time in the $g'r'$ channels. The latter cannot be precisely known because of the not exactly predictable overhead of a FIERA exposure. As the dark current is negligible in the CCDs, this trade-off is justified. For very short exposures of very bright targets a fast readout mode is also provided, which reduces the readout time from 46 s to 4.4 s.

The NIR chips are operated normally. The three chips with four amplifiers each are treated as 12 video channels and are stored in a single frame. This implies that all three chips must

be read out together. As a consequence, the efficiency of the JH channels are slightly reduced: This is because the integration time for faint targets is limited by the sky brightness in the K band to ~10 s while the other two bands could, in principle, integrate longer. This results in a 2 s overhead. In addition, the JH chips must also wait for the dither mirror movements, resulting in an additional 0.5 s overhead for each mirror movement. There is no additional readout noise due to the larger number of JH reads because the total noise is dominated by the Poisson noise of the sky background.

The two arms (optical and NIR) are operated in semiparallel. Both detector systems are started independently consecutively (within milliseconds) and the requested number of frames are taken with as little dead time as possible. In general the two detector systems are *not* synchronized—except after telescope slews.

The instrument control software has no provisions to fill the time available between telescope movements. It is the user's responsibility to request the optimal number of exposures. In order to ease this task, a few optimal configurations are offered.

Relatively frequent telescope offsets are required to be able to determine the sky variations in the J and H band (the K band is handled by the built-in dither mirror). in order to increase efficiency and to simplify usage, the dither pattern is a predefined circle—the user only defines the number of dither positions. GROND uses so-called "combined offsets"; i.e., guiding continues without operator interaction after a telescope offset. The operator is only required to select the guide star at the beginning of an OB.

Observations, both in visitor and service mode, are done through OBs. The user can use the normal p2pp tool (P2PP Manual 2007;[10] Comerón & Silva 2007) like for any ESO instrument (despite GROND not being an official ESO instrument). In the case of GRB observations, OBs are generated in real time by a special process. The input parameters are provided by the GROND pipeline host (see next section), which is translated into a standard OB. To reduce overheads, the instrument workstation always provides the current telescope pointing to the pipeline machine. Thus, the pipeline may conclude that the current pointing is "good enough" (i.e., the aim coordinate and error circle fall within the field of view of the optical CCDs) and skip the telescope preset. In this case guiding will continue without operator interaction, even when executing several OBs consecutively (guiding does not stop at the end of an OB). At the start of each OB, the instrument is focused by moving M2 (see § 5.3). As GROND is fine-tuned for GRB follow-up where speed is crucial, no manual focusing is foreseen before a GRB observation starts—but the necessary templates are available for standard observing runs.

[10] See http://www.eso.org/observing/p2pp/P2PP-tool.html#Manual.

To make data analysis easier, all images produced by GROND contain important information in the FITS headers. Thus, the images can be fed into standard software such as IRAF as the required header cards describing the bias/trim/overscan regions and amplifiers are included. The visual channels are also identified by the header ($g'r'i'z'$); the infrared channels are in one image (see above). Obviously, all other relevant parameters (gain, readout noise, etc.) are also included for each chip in the header.

Crude astrometry (WCS cards) is also included in each image. In the optical the astrometry is correct, apart from a shift introduced by the pointing of the telescope. The astrometry is correct for all chips (i.e., individual chip shifts, rotations, etc. are included). As there are no significant distortions in the optical channels, the astrometry is very accurate (0.2″)—once the pointing origin is fixed. In the NIR channels, the astrometry does *not* include the focal plane distortions (which is significant due to the focal reducer). Furthermore, the NIR detector system produces a single image so an extra processing step is required to slice the image into the three bands and to extract the necessary information from the header. The header cards also take into account the K-band dithering mirror position.

4.2. The GROND Pipeline I: Observation Scheduling

The GROND Pipeline (GP) system is a software package designed and written specifically for GROND. Its prime objective is to schedule rapid GRB afterglow observations (part I; described in this section) and determine the redshift as quickly as possible (part II; described in § 4.3). All the components of the GP are deployed on a PC—the so-called pipeline machine—which is located in the telescope building.

The coordinates of a GRB are distributed to the world through the Gamma-ray bursts Coordinates Network (GCN) in a few seconds (Barthelmy et al. 2000). GROND reacts to GCN notices. The architecture of the GP is based on an asynchronous framework to provide the speed and the degree of freedom necessary to apply different analysis strategies. In the context of the GP system, asynchrony means that all tasks of Table. 1 are distributed among different processes that do not run sequentially but asynchronously.

The GP mainly consists of two layers, the system layer and the GRB analysis layer (see Table. 1). The system layer consists of the processes that receive the GRB alerts, decide whether to follow that burst or not, schedule and reschedule observations and conduct the observations by initiating, continuing, interrupting or ending them. Furthermore, the main system process controls all processes, including the analysis processes, and coordinates the interprocess communication. The GRB analysis layer contains preprocessing of the images, photometric analysis, identifying the GRB afterglow, spectral energy distribution (SED) analysis, and photometric redshift determination.

The details of the processes are described in a separate paper (Yoldaş et al. 2008, in preparation).

TABLE 1
THE DUTIES OF THE SYSTEM AND THE GRB ANALYSIS LAYERS OF THE GP.

System—Observation Control Layer	GRB Analysis Layer
Receiving GRB alerts	Preprocessing the images
Deciding whether to observe the target	Photometric analysis of 7-band data
Calculating visibility of the target	Constructing the SED of the objects
Scheduling of the observations	Identifying the GRB afterglow
Triggering/continuing/stopping observations	Determining the photometric redshift
Providing web-interface for user interaction	Evaluating the accuracy of the redshift

4.2.1. Receiving GRB Alerts

When a GRB alert comes in via the GCN socket connection,[11] the main process extracts all the information from the packet by parsing it according to its type. It first checks whether it is a packet for an existing GRB or a new target for the system. Then the decision tree splits according to packet types. Based on this information and the predefined user decision on the target type, the system decides whether to follow up. For a new target, the visibility of the target is calculated independent of the autonomous decision of the software to follow or not. The visibility calculations utilize *skycalc*, a C program written by John Thorstensen,[12] with a python wrapper. The visibility of the object is normally calculated for the given/current time or the upcoming night. If it is observable and does not conflict with other checks (e.g., Moon distance), then it is scheduled for observation. Scheduling means that the main process prepares an observation plan of the target (which typically will contain several OBs, possibly also of different lengths), satisfying the above-defined criteria, and tries to schedule it with the other observation plans, if any exist.

4.2.2. Scheduling of Observations

The scheduling of observations for GROND needs to be fully automated like the other parts of the system, but at the same time it should allow users to modify, add, and delete the scheduled observations. Furthermore, the automatically scheduled observations may be deleted by the system, as a result of a "Retraction" or a later "Ignore" decision derived from the GCN packets for that target.

Some of the other robotic or automated telescope systems, e.g., the Liverpool telescope (Guidorzi et al. 2006), use "just in time" (JIT) scheduling, which is based on choosing the observation to be conducted instantly at every time rather than scheduling a set of observations for a whole night. JIT scheduling is not suitable for GROND because (i) ideally, all GRBs that occur on the same night and that are visible should be observed; however, JIT scheduling does not allow the system to foresee the night and hence arrange the observation durations accordingly; (ii) the user should be able to interact with and modify the schedule, e.g., to implement other priorities based on other information (short duration GRB, or GRB at high redshift); and (iii) GROND shares the telescope with two other instruments for which the observers and operators want to know the schedule of the upcoming hours. Therefore, we developed our own scheduling system that fulfills all the requirements of GROND. The resolution of conflicts between competing observation plans is done based on a priority scheme. By definition, at the times when the planned observations need to be rescheduled, the observation plan with higher priority can partially or totally override another observation plan with lower priority. For GP, the latest burst has the highest priority. However, the users can also change the priority of any observation.

4.2.3. Automating the GRB Afterglow Observations

When the start time of an observation is confirmed, the GP system triggers the Rapid Response Mode (RRM[13]) by sending the coordinates of the target and the name of the observation block to be used to a dedicated directory. The RRM procedure has been widely used for the VLT, and was implemented at the La Silla site for GROND operations on the 2.2 m telescope. A RRM acquisition template ends any ongoing observation, slews the telescope, and sets up GROND. After the RRM trigger, the next observation blocks are sent directly via the Instrument Work Station (IWS), rather than the dedicated RRM directory. Because the GP system does not have direct control over the GROND instrument, commands and OBs are relayed through the IWS using a specifically designed communication protocol. Once the RRM is accepted, the main process of the GP system creates a GRB process called GRBServer. This GRB process controls several subprocesses, responsible for the analysis of all the 7-channel images obtained for that observation, created by typically several subsequent OBs.

4.3. The GROND Pipeline II: Analyzing GRB Afterglow Observations

The analysis of GROND GRB afterglow observations are conducted on the fly, managed and controlled by the GP system. When an observation is executed, images appear in a certain directory, as the data handling system (DHS) of ESO pulls them from the IWS and stores them in a data directory on the pipeline machine. The analysis of each image starts immediately after it appears in the data directory.

The steps of the data analysis depend on the structure of the OB and the choice of the analysis strategy by the users. In total 22 combinations of data analysis strategies utilizing 12 different processes are available. The aim is to construct as quickly as

[11] See http://gcn.gsfc.nasa.gov/gcn_describe.html.
[12] See ftp://iraf.noao.edu/contrib/skycal.readme.
[13] See http://www.eso.org/observing/p2pp/rrm.html.

possible a spectral energy distribution (SED) of the target object to determine its photometric redshift.

In all strategies, the single band images are corrected for the dark current and bias, introduced by the detector and detector electronics, and the multiplicative effects, i.e., the pixel-to-pixel sensitivity and the illumination variations across the image. The remaining steps, including (i) correction for the geometrical distortion introduced by the focal reducer lenses in front of the infrared detectors, (ii) sky subtraction for the infrared images, and (iii) shifting and adding of the images obtained at different telescope positions (dithered), vary depending on the strategy. Overall, different strategies can be grouped into two, depending on when the astrometric and photometric analyses are conducted. The astrometry and photometry can be conducted either only on the images acquired at the same telescope position, or at the end of an OB. All the analysis processes until the identification of the GRB afterglow utilize Pyraf/IRAF libraries.[14] Astrometry is done by matching the objects detected in the images with those that are in the optical or infrared catalogs, namely USNO A-2, USNO B1, DENIS, 2MASS, NOMAD, and GSC22, which are downloaded via the Internet.[15]

The objects found in each of the 7 bands are matched based on their world coordinates, after the photometric analysis. The result of the match gives us SEDs of all the objects detected in an OB. The identification of the GRB afterglow among the many objects detected in the image is based on a figure-of-merit approach. Marks are given to each object as a result of several tests, namely whether (i) the object is inside the area given by the gamma, X-ray, or optical position uncertainty distributed by GCN packets, (ii) the coordinates of the object match with any object in the catalogs, (iii) the magnitudes of the object show variability in time, and (iv) the colors of the object resemble those of other GRB optical or infrared afterglows (Rhoads 2001).

Before the SEDs of the best candidates are analyzed by the publicly available HyperZ code (Bolzonella et al. 2000), they are first tested for a Ly break. A single and a broken power-law model are fit to the SED of each object, and three tests are applied on the results of these fits in order to decide whether the Ly break is covered by the data. The redshift range that can be observed by GROND is $z \sim 3.5$–13. The HyperZ tests we conducted with simulated and real afterglow data showed that HyperZ is able to determine the redshift with an accuracy of $\Delta z \sim 0.3$–0.5 (see Fig. 13), if the data cover the Lyman feature.

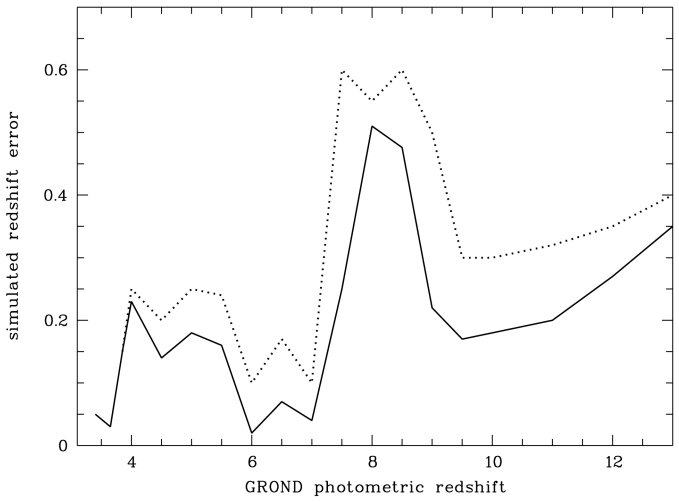

FIG. 13.—The error in GROND's photometric redshift determination of GRB afterglows is expected to be smaller than ± 0.3 for most of the redshift range. Only for redshifts where the Ly break falls between the z' and J bands, i.e., $z \approx 8$, does the accuracy disimprove. The solid line shows the simulated error in redshift when assuming ± 0.5 mag relative photometric accuracy between the seven bands. The relatively good performance around $z \sim 6$ is due to the narrow i' band in GROND. The dotted line shows the (larger) error when in addition one assumes an intrinsic GRB host extinction of $A_V = 1$ that is not accounted for in the fit. For low redshifts there is hardly any difference since the NIR bands provide a precise lever arm.

5. GROND AT THE 2.2 M TELESCOPE

The 2.2 m MPI/ESO telescope is the obvious first choice for GROND. In order to detect a large fraction of GRBs, a 2 m class telescope is a minimal requirement. Working within the ESO environment would allow follow-up observations at the VLT with rather simple procedures as well as providing the (European) GRB community with unique data. Moreover, it was expected that the pressure on the 2.2 m MPG/ESO telescope might decrease once VST and VISTA become operational.

5.1. M3

In order to produce the smallest possible impact on the operation of the other two instruments on the 2.2 m telescope, the Wide Field Imager (WFI[16]) and the fiber-fed Echelle spectrograph FEROS,[17] we designed a movable M3 mirror which, in case of a GRB alert, is folded in and reflects the light off toward the side of the telescope (Coudé-like focus) where GROND is permanently mounted. This leaves the common-user instruments WFI and FEROS unaffected at the Cassegrain focus of the telescope. Since GROND observations start as soon as

[14] IRAF (see iraf.noao.edu) is a data reduction and analysis software package of NOAO, and Pyraf (see http://www.stsci.edu/resources/software_hardware/pyraf) is a Python wrapper for IRAF, provided by the Space Telescope Science Institute.

[15] We used the VizieR gateway at http://vizier.u-strasbg.fr/viz-bin/VizieR.

[16] For more information on the WFI, see http://www.ls.eso.org/lasilla/sciops/2p2/E2p2M/WFI/.

[17] For more information on FEROS, see http://www.ls.eso.org/lasilla/sciops/2p2/E2p2M/FEROS/

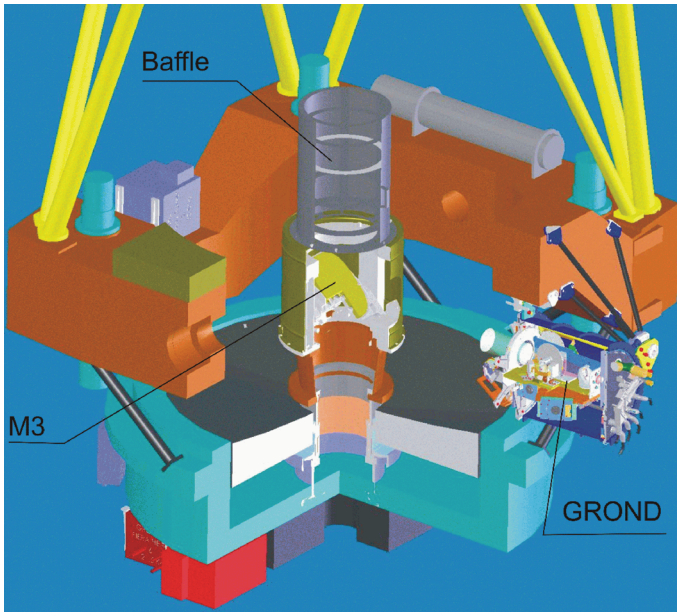

FIG. 14.—Cutout view of GROND at the telescope with the new M3 within the light baffle.

possible after a GRB alert, the switching mechanism had to be fast, rigid, and reproducible in its alignment.

The M3 mirror itself has an elliptical shape with a dimension of $492 \times 324 \times 60$ mm^3. The dimensions of the mirror are large enough to guarantee that additional off-axis light is available for a guiding camera sitting on top of the GROND vessel (see § 5.4). The mirror consists of CeSIC (carbon-fiber reinforced silicon carbide). The advantage of this material for our application is its low density and high rigidity so that the weight of the M3 mirror is only 8.2 kg; the mass of the total movable part is 23.5 kg. Also, this material allows the mirror and support structure to be thin enough that no obstruction occurs when in the upright position for WFI or FEROS observations.

The complete M3 mirror system (Fig. 14) can be switched to the GROND position within about 20 s. The accuracy of the alignment with the optical axis was tested several times and found to be better than 10″.

5.2. Pointing Model

Due to the very asymmetric position of the GROND cryostat vessel on one side and the electronics on the opposite side of the telescope centerpiece, a new pointing model had to be created using the TPOINT package (Wallace 2007). In addition to the components used for the Cassegrain instrumentation, two new components (HCEC and HCES, both unrelated to the GROND assembly, but correcting an earlier omission) were added in modeling the offsets of the 100 stars that had been measured at different azimuth and elevation angles. The effect of GROND on the pointing model is absorbed by those components that had already been implemented (most notably the fork flexure and the tube flexure). The resulting pointing model leaves an rms scatter of 5″ for both GROND and WFI (without the compromise of ensuring a good WFI/FEROS pointing it would be $\lesssim$2″).

5.3. Pointing-Direction–Dependent Focus

Due to the location of the GROND camera on the centerpiece, the bending of the telescope at different sky positions introduces a variable focus change. This focus change only depends on the declination, because bending in the plane of the telescope fork only leads to a lateral displacement of the beam away from the optical axis, not a focus change. The focus changes correspond to about 60 μm of M2 movement between zenith and 70° zenith distance, as compared to the 66 μm focus change induced by a 1° temperature change. Switching in or out the M3 mirror reproduces the focus to within ± 8 μm. Automatic refocusing has been implemented at the template level and thus is executed at each start of an OB. In addition to the temperature T, the focus formula ($\mathrm{F} = \mathrm{const.} - 66\mathrm{T} - 80\cos(\mathrm{DD})$; in units of μm) accounts for the telescope position in the North-South direction (DD is the declination difference relative to zenith).

5.4. Guiding

In accordance with ESO standards it was mandatory for GROND to be equipped with a guide camera. In order to ease integration with the existing telescope control system. the "New Generation Technical CCD" (NGTCCD[18]) system of ESO with a 1 K $\times$ 1 K E2V chip was implemented. In view of the semi-robotic operation, a field of view large enough to always contain a star brighter than $V \sim 15$ mag was deemed necessary. Therefore, the f/8 beam of the telescope was reimaged to yield a 0.33″ pixel^{-1} plate scale, and a FOV of 5′ across. The NGTCCD was placed outside of the main GROND vessel, and is fed by a pick-off mirror (M4) next to the entrance window of GROND (Fig. 15). A folding mirror (not shown in Fig. 15) is introduced between the triplet lens system and the detector to ease mounting on the GROND vessel. The M4 pick-up mirror is a weakly spherical mirror (80 km radius of curvature) that is slanted by 2° relative to a standard symmetric use, thus minimizing astigmatism. The triplet lens system adapts the plate scale to the chosen detector (pixel size and number). The guide camera's FOV is located 23′ south of the main GROND imaging FOV.

6. CALIBRATION AND PERFORMANCE

GROND was mounted at the 2.2 m telescope in April 2007 (Fig. 16), and saw first light on the sky on April 30 (Fig. 17).

[18] The manual for the VLT Software is found at ftp://ftp.eso.org/pub/vlt/vlt/pub/releases/JAN2006/vol-4/VLT-MAN-ESO-17240-3558.pdf.

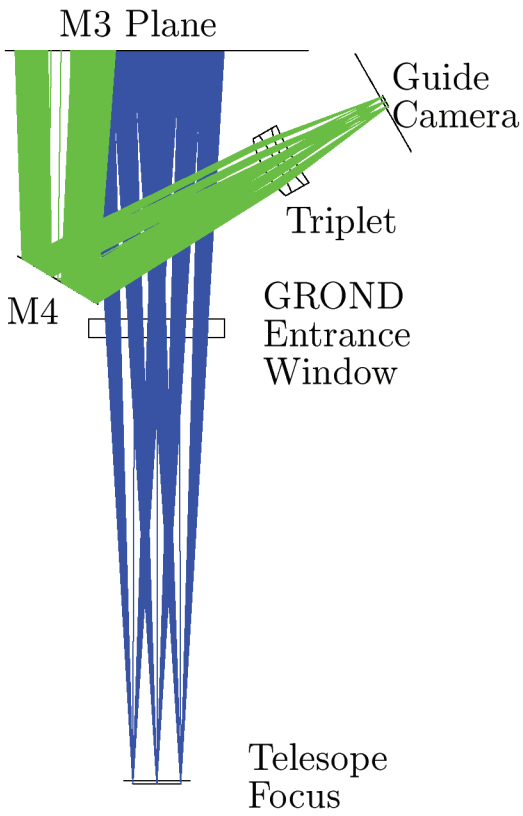

FIG. 15.—Layout of the guide camera, with the M4 pick-off mirror next to the entrance window.

GROND has been running smoothly since. Particularly noteworthy are three effects: (i) there has been no need for continuous pumping; the CCC acts as a cryopump, and keeps the vacuum stable at $\approx 5 \times 10^{-8}$ mbar; (ii) the NIR detector focusing stages remained stable within the depth of focus over the first few months; (iii) no effects of flexure have been recognized.

First calibration observations included the derivation of zero points for all seven bands, checks for vignetting and flexure, the determination of the focus formula (see § 5.3), and the effect of the K-band dither mirror.

6.1. Efficiency and Limiting Magnitudes

Best possible efficiency has been a driver of many decisions during the development of GROND, including special sensitization of the four CCDs for their respective wavelength band, silver (rather than aluminum) coatings of the various mirrors, and stringent transmission requirements of the dichroics and antireflection coatings. The efficiencies of the various elements in the optical path, including the telescope mirrors, are shown in Figure 18. The total efficiency in the visual bands is at the 70% level (except the z' band), and still above 50% for the three NIR bands. We note here that the combination of dichroics and JHK filters leads to a very high efficiency in GROND's NIR part despite the 11 lenses per channel and the comparatively low quantum efficiency of the Hawaii detectors.

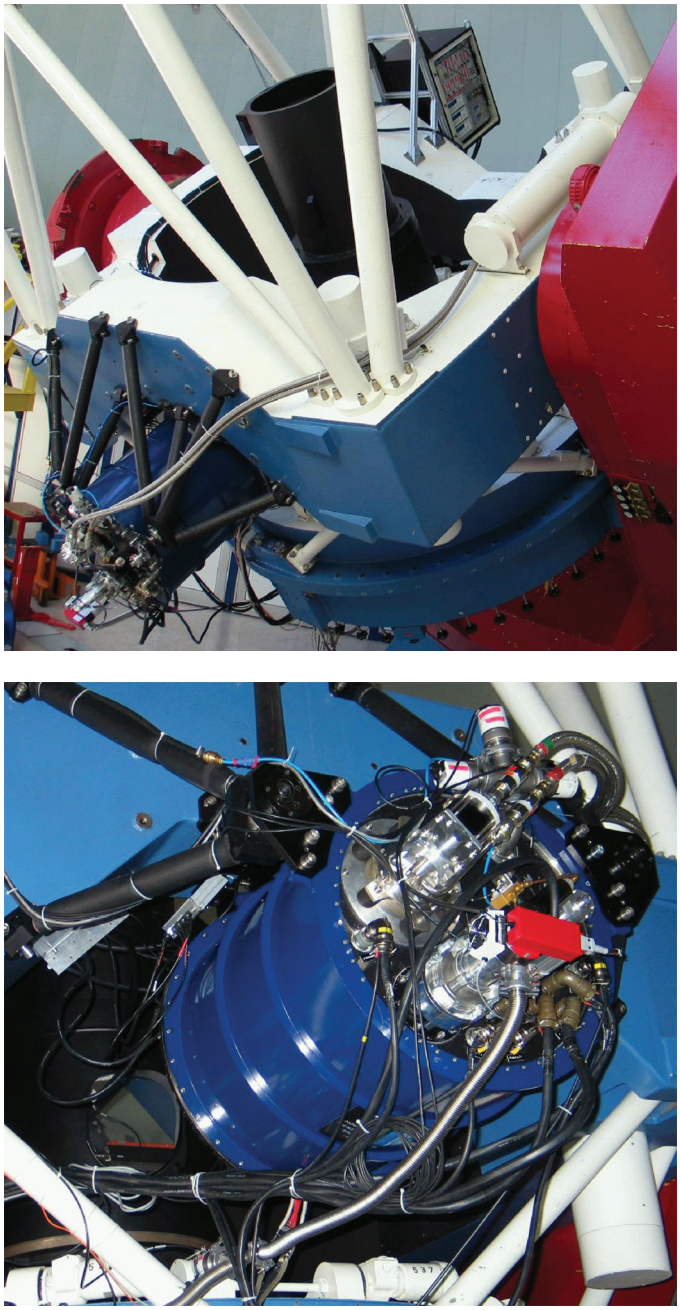

FIG. 16.—The GROND instrument at the 2.2 m telescope. *Left:* Grand view of the telescope, GROND to the lower left, the light baffle on top of M3 in the middle, and the main electronics rack at the top. *Right:* Blow-up of the GROND vessel and its various connections. The backside of the cryostat contains the CCC, the turbo-molecular pump, as well as a small emergency pump for rare cases of power outages.

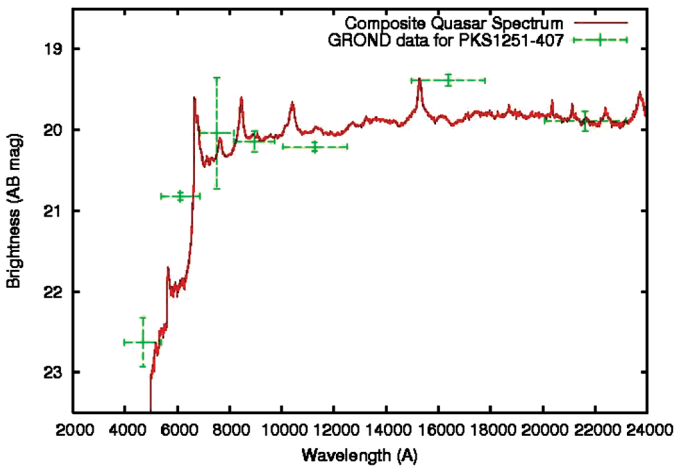

FIG. 17.—First scientific demonstration result from 2007 April 30,: green crosses are the GROND camera photometric estimates as derived from a 8 minute observation block of the quasar PKS 1251-407. The derived photometric redshift is $z = 4.44$, compared to the spectroscopic redshift of $z = 4.46$. The red line is the composite quasar spectrum from Francis et al. (1991).

Photometric zero points were determined by observing Landolt stars SA114-750, SA114-656 in all seven channels and SA114-654 in the near-infrared at many different air masses (Landolt 1992). In the $r'i'z'$ bands the inherent photometric accuracy is 0.5% and 1% in the g band (magnitudes are consistent at this level in a single OB). Long-term (spreading two photometric nights) and air-mass dependencies in all four visual bands are shown in Figure 19, demonstrating that GROND is capable to perform below 1% accurate photometry. The measured extinction coefficients are 0.182 ± 0.003, 0.121 ± 0.005, 0.061 ± 0.007, and 0.044 ± 0.006 in the g', r', i', and z' band, respectively.

The main reason GROND cannot deliver absolute photometry at this level in the visual bands is the lack of calibration standards *in the native GROND system*. Both SA-114 stars used are primary SDSS standards (Smith et al. 2002). The spectral types of both stars are also known (Drilling & Landolt 1979, Cohen et al. 2003). Using spectral templates from calspec/STSCI and Pickles (1998), we estimated the magnitudes of these two stars in the native GROND system. The combined effect of the photometric accuracy of the primary SDSS standards and our conversion limits the achievable overall accuracy in the r', i', and z' band to 1%. In the g band, the accuracy is limited to 5%. This is due to the fact that the camera has a significantly better response in the UV, as expected. Thus, the system becomes undefined below 3500 Å, and the magnitudes cannot be converted to the native system of the instrument. To demonstrate that the g' band can perform just as accurately, we introduced an external UV filter temporarily that cuts all UV flux. With this correction, the accuracy of the g' band is also around 1%—slightly worse than the other three bands as the templates used are

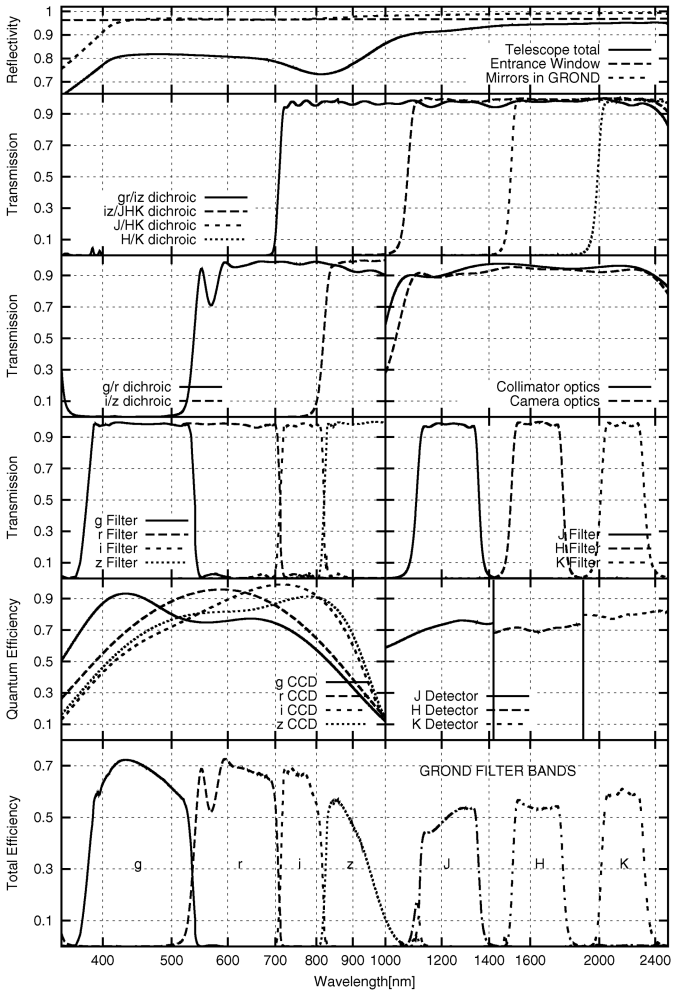

FIG. 18.—Efficiency of the GROND instrument at the 2.2 m telescope. *Top panel:* telescope and GROND-internal mirrors. *Panels 2 and 3 from top:* transmission of the dichroics, NIR lens systems. *Panel 4:* Transmission of the filters. *Panel 5:* Detector quantum efficiencies. *Bottom panel:* Total efficiency in each of the seven GROND bands. All losses are included, except the obstruction of M1 by M2. Except for the telescope (M1, M2) data, all curves represent measured data at their operating temperatures, i.e., all transmission values for the lenses, dichroic and antireflection coatings refer to 80 K. The measured efficiency in all seven bands on the sky turns out to be within 10% of the one expected from the bottom panel.

not sufficiently accurate around the 4000 Å break. Unfortunately the optical quality of our UV filter was so bad that it prevents scientific use. Consequently, a filter has been introduced in the camera in 2008 March.

In the NIR bands, magnitudes are only accurate to 3% in single (10 s) frames. Due to the significantly lower accuracy and the significantly lower extinction coefficients (which are water-content–dependent in any case—i.e., they are different every night) the NIR performance can only be determined by observing long-term trends. Currently we accept zero points of 22.97, 22.22, and 21.51 in J, H, and K, respectively, for 1 s integration time and air mass of 1 (see Table 2). Until more

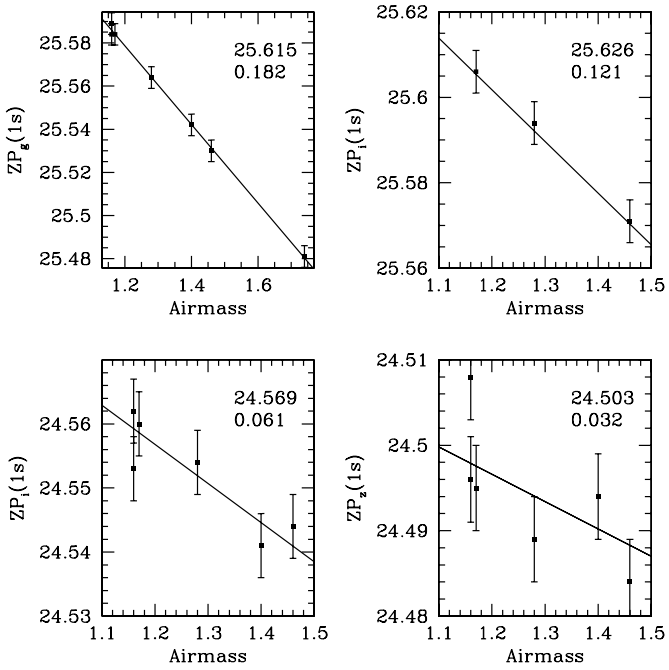

FIG. 19.—Air-mass dependence of the photometric zero point in the visual bands. Magnitudes are in the AB system and the zero point is calculated for 1 s integration and for ADU (i.e., not electrons). The extinction coefficients and the extrapolated zero point at an air mass of 1 are shown for all four bands.

data is collected, we will use nominal extinction coefficients of 0.12 (J), 0.06 (H), and 0.07 (K).[19]

6.2. Photometric System Transformations

A first set of calibration observations was performed in 2007 mid-July, though not in photometric conditions. Thus, the constants in the following equations may change slightly (see www.mpe.mpg.de/~jcg/GROND for updates).

First, we derive transformation equations between the GROND (G) visual bands and the Sloan (S) filter system:

$$g'_{\rm G} = g'_{\rm S} + (0.000 \pm 0.001) + (0.105 \pm 0.014) \times (u' - g')_{\rm S} + (0.036 \pm 0.024) \times (g' - r')_{\rm S}$$

$$r'_{\rm G} = r'_{\rm S} + (-0.001 \pm 0.001) + (0.056 \pm 0.011) \times (g' - r')_{\rm S} + (-0.089 \pm 0.022) \times (r' - i')_{\rm S}$$

$$i'_{\rm G} = i'_{\rm S} + (-0.001 \pm 0.001) + (-0.029 \pm 0.007) \times (r' - i')_{\rm S} + (0.004 \pm 0.011) \times (i' - z')_{\rm S}$$

$$z'_{\rm G} = z'_{\rm S} + (-0.001 \pm 0.001) + (0.034 \pm 0.003) \times (i' - z')_{\rm S}.$$

Next, the transformations between the GROND NIR bands and the 2MASS (2M) system are as follows:

$$J_{\rm G} = J_{\rm 2M} + (-0.003 \pm 0.001) + (0.005 \pm 0.001) \times (J - H)_{\rm 2M}$$

$$H_{\rm G} = H_{\rm 2M} + (0.002 \pm 0.001) + (0.021 \pm 0.001) \times (J - H)_{\rm 2M}$$

$$K_{\rm G} = K_{\rm 2M} + (-0.003 \pm 0.001) + (0.094 \pm 0.003) \times (J - K)_{\rm 2M}.$$

For transformation from 2MASS to other systems, see Carpenter (2003).

Finally, the transformations between the visual GROND bands and the WFI (W) system are

$$g'_{\rm G} = B_{\rm W} + (0.001 \pm 0.012) + (0.132 \pm 0.022) \times (U - B)_{\rm W} + (-0.127 \pm 0.053) \times (B - V)_{\rm W}$$

$$r'_{\rm G} = V_{\rm W} + (0.001 \pm 0.001) + (0.039 \pm 0.023) \times (B - V)_{\rm W} + (-0.852 \pm 0.024) \times (V - R)_{\rm W}$$

$$i'_{\rm G} = R_{\rm W} + (0.016 \pm 0.003) + (-0.163 \pm 0.046) \times (V - R)_{\rm W} + (-0.485 \pm 0.044) \times (R - I)_{\rm W}$$

$$z'_{\rm G} = I_{\rm W} + (0.012 \pm 0.002) + (-0.089 \pm 0.005) \times (R - I)_{\rm W}.$$

Only for the r' band we reach a residual 1% rms scatter, while for i' and z' the residual rms scatter is 2%. For a transformation to the standard Landolt (Johnson BV and Cousins RI) system see the dedicated WFI Web page.[20]

7. SUMMARY

GROND is an imaging system capable of operating in seven colors simultaneously. It has been designed and built at MPE Garching, and commissioned at the 2.2 m MPI/ESO telescope on La Silla, Chile. First observations show that all properties are according to specifications and expectations. The first observations of gamma-ray bursts with GROND have also been obtained (Greiner et al. 2007a,2007b; Primak et al. 2007, Krühler et al. 2007). Fine-tuning of the operations strategy as well as scheduling and analysis software in the upcoming weeks is expected to bring GROND into a fully operational condition, thus allowing the commencement of normal science operations.

We thank K. Meisenheimer, R.-R. Rohloff and R. Wolf (all MPIA Heidelberg) for their support in getting the telescope

[19] Updates of these performance values will be posted at http://www.mpe.mpg.de/~jcg/GROND/.

[20] The Web page is located at http://www.ls.eso.org/lasilla/sciops/2p2/E2p2M/WFI/zeropoints/.

TABLE 2

ZERO POINTS AND 3 Σ LIMITING MAGNITUDES FOR AN 8 MINUTE OBSERVATION BLOCK WITH FOUR TELESCOPE DITHER POSITIONS (CORRESPONDING TO AN EFFECTIVE EXPOSURE TIME OF 4×130 S IN THE VISUAL AND $4 \times 12 \times 10$ S IN THE NIR CHANNELS) FOR THE SEVEN GROND CHANNELS AT THE 2.2 M TELESCOPE. THE ERROR IN THE ZERO POINT IS ABOUT ± 0.03 MAG. THE LIMITING MAGNITUDES IN THE NIR ARE THE MEAN VALUES IN THE AB SYSTEM; THEY EXHIBIT SEASONAL VARIATIONS BY UP TO ± 0.5 MAG.

GROND	zero points (mag)		limiting magnitude
channel	Vega	AB	in 8-minute OB
g'	25.62	25.63	24.2
r'	25.47	25.62	24.2
i'	24.16	24.55	23.5
z'	23.99	24.51	23.3
J	22.97	23.88	21.1
H	22.22	23.60	19.9
K	21.51	23.30	18.3

interfaces right, and for FE computations of the M3 mirror rigidity. Particular thanks to the whole La Silla Observatory staff for their enthusiasm and effort during the assembly of all the GROND components to the telescope. We thank D. H. Hartmann (Clemson Univ.) for stimulating discussions, K. Garimella (formerly also Clemson Univ) and D. A. Kann (Tautenburg Observatory) for help in implementing SED-fitting routines as preparatory steps for HyperZ, as well as A. Rossi (Tautenburg Observatory) for support in the derivation of the photometric conversion equations. We are grateful to the anonymous referee for the many detailed comments which improved to readability and consistency of the paper. We greatly acknowledge the special efforts of the following companies to fulfill our often unusual requirements: Berliner Glas KGaA, ECM Moosinning, FEE GmbH Idar-Oberstein, Korth Kristalle GmbH Altenholz, Laseroptik GmbH Garbsen, Laser Zentrum Hannover e.V., Präzisionsoptik Gera, Steinbach-Könitzer-Lopez Jena, Tafelmaier Dünnschichttechnik Rosenheim. Part of the funding for GROND (both hardware as well as personnel) was generously granted from the Leibniz-Prize (DFG grant HA 1850/28-1) to G. H. (MPE).

REFERENCES

Barthelmy, S. D., Cline, T. L., & Butterworth, P., et al. 2000, in AIP Conf. Proc. 526, ed. R. M. Kippen, R. S. Mallozzi, & G. J. Fishman (New York: AIP), 731

Beletic, J. W., Gerdes, R., & Duvarney, R. C. 1998, Optical Detectors for Astronomy : Proceedings of an ESO CCD Workshop Held in Garching, Germany, October 8–10, 1996, ed. J. W. Beletic, & P. Amico (Dordrecht, Boston: Kluwer), 228, p. 103 (see also www.eso.org/projects/odt/Fiera)

Bolzonella, M., Miralles, J.-M., & Pelló, R. 2000, A&A, 363, 476

Carpenter, J. M. 2003, www.astro.caltech.edu/~jmc/2mass/v3/transformations/

Chavan, A. M., Silva, D. R., Boarotto, C., Canavan, T., Kemp, R., & Giannone, G. 2000, Proc. SPIE, 4010, 81

Cohen, M., Megeath, S. T., & Hammersley, P. L., et al. 2003, AJ, 125, 2645

Comerón, F., & Silva, D. 2007, P2PP (Phase2 Proposal Preparation) Manual vol. 2.13, issue 9, Doc. No. VLT-MAN-ESO-19200-1644

Depoy, D. 1998, URL www.astronomy.ohio-state.edu/~depoy/research/instrumentation/andicam/andicam.html

Dhillon, V. S., et al. 2007, MNRAS, 378, 825

Drilling, J. S., & Landolt, A. U. 1979, AJ, 84, 783

Dunham, E. W., Elliot, J. L., & Bida, T. A., et al. 2004, Proc. SPIE, 5492, 592

Ellis, T., Drake, R., Fowler, A. M., Gatley, I., Heim, J., Luce, R., Merrill, K. M., Probst, R., & Buchholz, N. 1992, Proc. SPIE, 1765, 94

Francis, P. J., et al. 1991, ApJ, 373, 465

Fukugita, M., Ichikawa, T., & Gunn, J. E., et al. 1996, AJ, 111, 1748

Gehrels, N., Chincarini, G., & Giommi, P., et al. 2004, ApJ, 611, 1005

Greiner, J., Clemens, C., & Krühler, T., et al. 2007a, GCN Circ. 6449, http://gcn.gsfc.nasa.gov/gcn/gcn3_archive.html

Greiner, J., Clemens, C., & Krühler, T., et al. 2007b, GCN Circ. 6694, http://gcn.gsfc.nasa.gov/gcn/gcn3_archive.html

Guidorzi, C., Monfardini, A., & Gomboc, A., et al. 2006, PASP, 118, 288

Hadad, N., & Sinclair, P. 1998, Optical Detectors for Astronomy : Proceedings of an ESO CCD Workshop Held in Garching, Germany, October 8–10, 1996, ed. J. W. Beletic, & P. Amico (Dordrecht, Boston: Kluwer), 228, p. 131 (see also www.eso.org/projects/odt/Fiera)

Jewitt, D. C. 2002, AJ, 123, 1039

Jha, S., et al. 2000, ApJ, 540, L45

Kann, D. A., Klose, S., & Zhang, B., et al. 2008, ApJ, submitted (astroph/0712.2186)
Kotani, T., et al. 2005, Nuovo Cimento C, 28, 755
Krühler, T., Greiner, J., Afonso, P., Küpcü-Yoldas, A., Yoldas, A., & Szokoly, G. 2007, GCN Circ. 7021, http://gcn.gsfc.nasa.gov/gcn/gcn3_archive.html
Landolt, A. U. 1992, AJ, 104, 340
Lamb, D. Q., & Reichart, D. E. 2000, ApJ, 536, 1
Laux, U. 1999, Astrooptik, Sterne und Weltraum, München: Verlag, 2nd ed.
Meyer, M., Finger, G., Mehrgan, H., Nicolini, G., & Stegmeier, J. 1998, Proc. SPIE, 3354, 134 (see also www.eso.org/projects/iridt/irace)
Orosz, J. A., & Bailyn, C. D. 1997, ApJ, 477, 876
Paczynski, B. 1986, ApJ, 304, 1
Pickles, A. J. 1998, PASP, 110, 863
Primak, N., Szokoly, G., & Greiner, J., et al. 2007, GCN Circ. 6590, http://gcn.gsfc.nasa.gov/gcn/gcn3_archive.html
Reif, K., Bagschik, K., & de Boer, K. S., et al. 1999, Proc. SPIE, 3649, 109
Rhoads, J. E. 2001, ApJ, 557, 943
Ritchey, G. W. 1928, JRASC, 22, 207
Roth, M. M., et al. 2006, PASP, 117, 620
Smith, J. A., et al. 2002, AJ, 123, 2121
Taubenberger, S., et al. 2006, MNRAS, 371, 1459
Vreeswijk, P., Ledoux, C., & Smette, A., et al. 2007, A&A, 468, 83
Wallace, P. T. 2007, www.tpsoft.demon.co.uk
Watanabe, M., Nakaya, H., & Yamamuro, T., et al. 2005, PASP, 117, 870
Woche, M. F., Laux, U., & Papamastorakis, J. 2000, Proc. SPIE, 4008, 930